LAWRENCE
LIVERMORE
NATIONAL
LABORATORY

LLNL-TR-661937

Stimulated Raman Scattering Inside KDP Crystal Segments - II

W. L. Smith, F. P. Milanovich, M. A. Henesian

October 3, 2014

Disclaimer

This work performed under the auspices of the U.S. Department of Energy by Lawrence Livermore National Laboratory under Contract DE-AC52-07NA27344.

February 25, 1983
UVM 83-03/3116T

TO: Distribution

FROM: W. Lee Smith, F. P. Milanovich, and M. A. Henesian

SUBJECT: STIMULATED RAMAN SCATTERING INSIDE KDP CRYSTAL SEGMENTS - II

In Laser R & D memorandum UVM 82-19[1] of August 25, 1982, information was presented which indicated the possibility of significant loss by stimulated Raman scattering (SRS) in the KDP harmonic crystal arrays on Novette and Nova. It was soon after agreed that we should extend this investigation by directly measuring the stimulated gain coefficient for SRS in KDP. We have done so, and this memorandum contains the results.

In Section I we describe a picture of the overall Raman scattering behavior of KDP that we have developed from a raft of additional spontaneous measurements made since November. In Section II we describe the absolute SRS measurements and arrive at the values for the gain coefficients. In Section III we examine the effect of these final numbers on the Nova/Novette arrays. A summary is given on page 20.

The authors thank R. B. Lopert for providing his wavemeter, acknowledge the expert contributions of C. L. Vercimak in the stimulated gain measurements, and thank T. G. Janssen for handling this manuscript.

W. Lee Smith

W. Lee Smith

Fred P. Milanovich

F. P. Milanovich

Mark A. Henesian

M. A. Henesian

WLS/MAH/FPM/tj

STRATEGY

The steps in this investigation were driven by the fact that no large laser system was available for this work. The Cyclops laser generates ∿ 3 J maximum at 526 nm (1 ns) inadequate for making a quality SRS gain coefficient in the transversely-pumped configuration, which is the actual geometry of the array. The Cyclops laser is quite adequate for making a quality measurement with collinear pump and probe beams, however. So our strategy was to (a) check out the Raman behavior (angle dependencies) of a simple Z-cut crystal using the spontaneous scattering apparatus, (b) predict from (a) and then measure the Raman behavior in a Type-II cut (θ = 59°) crystal on the spontaneous apparatus, (c) make absolute stimulated gain measurements on Cyclops in a number of crystal orientations and compare with the spontaneous-scattering model, and (d) from the above sets of data, extract the gain coefficients relevant for Nova/Novette.

I. MEASUREMENT OF THE SPONTANEOUS RAMAN SCATTERING TENSOR OF KDP

In Ref.1 we pointed out that the Raman mode of concern in KDP is at 915 cm^{-1}. When this project began, we understood[2,3] this mode to be a totally symmetric vibration, internal to the PO_4 subgroups having the customary designation ν_1. The locations of these tetrahedrally-shaped subgroups in the KH_2PO_4 unit cell, are shown in Fig. 1[4] and in Fig. 2, we show the "breathing" motion involved in the ν_1-mode vibration. The significance of the descriptor "totally symmetric" is that such a vibration cannot alter the polarization state of the light which is Raman scattered - there is no "depolarized" scattering. Hence this Raman process is described by a diagonal scattering tensor

$$S'_{ij} = \begin{bmatrix} a & 0 & 0 \\ 0 & a & 0 \\ 0 & 0 & b \end{bmatrix} \qquad (1)$$

where $a \neq b$ results from the symmetry of the unit cell.

Eq. 1 is a delightfully simple representation. Unfortunately, we found the Raman activity in KDP to be considerably more complex, requiring a tensor more of the form

$$S_{ij} = \begin{bmatrix} a & c & d \\ c & a & e \\ d & e & b \end{bmatrix} \qquad (2)$$

where all elements are nonzero.

The physical reason for the inadequacy of the simpler tensor (Eq. 1) becomes evident from a closer look at the KDP structure, using x-ray analysis. Fig. 3^6 is a view of the KDP unit cell looking down the optic (z) axis. In this figure the circles represent oxygen atoms, the dashed lines the hydrogens, and the potassium atoms are not shown. OH bonds attach to each corner of the PO_4 tetrahedra, thereby inter-connecting them. The important feature here is that the PO_4 tetrahedra are not oriented squarely in the unit cell. Each is rotated a small amount about the optic axis. We hypothesize that along with this rotation is the second-order effect that the PO_4 cage is distorted away from perfect tetrahedral shape. This results in the mixing together of the normal vibrational modes of the undistorted PO_4 unit, thereby giving a nonzero off-diagonal element c in Eq. (2).

If we look at Fig. 4, we see that there is no similar rotation of the PO_4 cage about the x or y axis. So, following our hypothesis, the second-order distortion to the PO_4 cage along the z direction should be smaller. Accordingly, tensor elements d and e should be much smaller than c.

To understand this crystal, given the above complexity, we measured the spontaneous Raman scattering strength in KDP for the entire set of possible orientations. This work was done on a conventional cw argon-pumped, double-monochometer Raman scattering spectrometer. A feature of this apparatus is that the collection optics look at 90° to the pump axis, so only side-scattering can be measured.

The Z-cut KDP crystal was 3x3x2 cm. The Type II crystal was 5x5x1.8 cm and was also used in some of the stimulated gain measurements. A significant improvement in the latest spontaneous measurements was the use of a glass tank containing index-matching fluid into which the crystal could be entirely submersed, to eliminate surface scattering and critical dependence of the scattering signal on sample position.

In Fig. 5 we show the lables for the crystalline axes that we will use throughout this memorandum. The crystalline axes are denoted x,y,z. Unit vectors along the sample edges (laboratory frame) are α, β, and γ. For keeping track of the numerous scattering configurations, it is very convenient to use Porto notation, that is,

A(BC)D

where A,B,C,D stand for unit vectors parallel to the

propagation direction of the input beam,
electric vector of the input beam,
electric vector of the Raman scattered light,
propagation direction of the Raman scattered light,

respectively. For example, $\gamma(\beta\beta)\alpha$ denotes a pump wave propagating along γ with polarization along β, scattered into a wave also polarized along β but propagating along α. That configuration would be for "polarized" (as opposed to de-polarized) side scattering. As additional relevant examples, $\gamma(\beta\beta)\gamma$ denotes polarized, forward scattering and $\gamma(\beta\alpha)\gamma$ denotes depolarized, forward scattering. A bar over a particular symbol denotes a "negative" direction.

Because it is the geometrically simpler of the two crystals, we will first describe the spontaneous scattering results for the z-cut crystal. In Table 1 we list the scattering configurations, the Raman tensor coupling of each, the Raman vibrational q-vector polar angle Ψ, and measured relative scattering strength for the 24 unique scattering configurations. The tensor elements are written to the second power as is appropriate for intensity; the scattering tensor introduced with Eq. 2 was written for amplitudes. The configurations are grouped according to

scattering plane, indicated by the outer two symbols of the Porto notation.

We see in Table 1 that the diagonal tensor elements a^2 and b^2 are the largest, making the scattering strength for polarized scattering stronger than for depolarized scattering. This much was expected. Within about 25%, the diagonal measurements are all equal. Yet, 25% is well outside our measurement uncertainty (± 5%).

It was at this point that our renewed literature search began to pay off. We found through an obscure reference and some phone calls a set of four papers[7-10] by Srivastava and coworkers at U. Utah on the angular dependence of Raman scattering in KDP. In Ref. 9, these workers reported a dependence of the diagonal element a^2 on the angle Θ between the directions of the incident and scattered light waves. This variation (a swing of 37%) is reproduced in Fig. 6. The angle Θ in Fig. 6 is identical to our usual phase-match angle. AT $\Theta = 59°$ (Type II SHG) we see that a^2 is about equal to its average value, also obtained at 0° or 90°. For this reason we have been able to ignore the dependence of a^2 on Θ for this memorandum. Note at 41° (for Type I SHG), $a^2(\Theta)$ is maximal.

In Ref. 7, Srivastava and Grow report a calculation of the gain coefficient for KDP relative to benzene, in the same manner as we did in Ref. 1. Their calculated result (converted to 526-nm pump) is 0.36 cm/GW, in fair agreement with our values. Unfortunately, Srivastava and Grow did not specify the orientation of the KDP crystal in their paper, and did not pursue quantitatively the impact of their other angle-dependent investigations on the stimulated gain.

As was already mentioned, it was unknown when we began this work that c^2, d^2, and e^2 would be nonzero. For scattering in the xz and yz planes, we found (Table 1) that the element c^2 is very close to 1/3 as strong as a^2. And we see that d^2 and e^2 are quite small - ignorable to first order. Depolarized scattering was reported by Popova and Stekhanov[11] in 1970. The other surprise in our spontaneous data was that c^2 is angle-dependent, vanishing for the x(yx)y and y(xy)x configurations, that is, for scattering in the xy plane. While at first we thought we had a new result here, we found this effect to be present but unnoted in the relative spectra published in another of Srivastava's papers.[8] This was a useful confirmation for our measurements.

We have incorporated the most important of the above features into a simple model for the first-order Raman activity of KDP. To explain, we need to introduce the q-vector of the Raman vibration, defined as the difference between the k-vectors of the pump and scattered light waves, $\vec{k}_p - \vec{k}_s$. For scattering in the xy plane, $\vec{q}$ is perpendicular to the optic axis of the crystal. By defining ψ to be the polar angle between $\vec{q}$ and the z-axis of the crystal, we arrive at an approximate form for the Raman tensor S_{ij} that includes all the first-order features:

$$S_{ij} = \begin{bmatrix} a & c(\psi) & 0 \\ c(\psi) & a & 0 \\ 0 & 0 & a \end{bmatrix} \qquad (3)$$

where

$$c(\psi) = a(2/3)^{1/2}|\cos\psi| \qquad (4)$$

For scattering in the xy plane, $\psi = 90°$ and c goes to zero, as measured. For the configurations $x(yx)\bar{z}$, $\bar{x}(xy)x$, $\bar{y}(xy)\bar{z}$, and $z(yx)\bar{y}$, ψ is approximately 45° (see Table 1), and $c(\psi)$ reduces to about $a/\sqrt{3}$, also as measured.

At this point we believed that we had a reasonable first-order model of spontaneous Raman scattering for this z-cut KDP crystal, and we proceeded to use it to predict what we should see for the other trial crystal which is Type-II cut. The comparison between the predicted and measured values for this crystal are shown in Table 2. For each scattering configuration, we list the full form for the effective scattering strength for each configuration, derived by transforming the applied electric field components into the crystal-axis frame, performing the Raman tensor multiplication, and then retransforming back to the laboratory frame. The approximate scattering strength from Eq. (3) and the angle ψ are also listed. For scattering in the $\gamma\alpha$ plane, ψ is given by

$$\cos\psi = \frac{k_p \cos\theta}{\sqrt{k_p^2 + k_s^2}} \qquad \underset{\sim}{k_p} = k_p \hat{\gamma} \qquad \underset{\sim}{k_s} = k_s \hat{\alpha} \tag{5}$$

and for scattering in the $\gamma\beta$ plane,

$$\cos\psi = \frac{k_p \cos\theta - k_s \sin\theta}{\sqrt{k_p^2 + k_s^2}} \qquad \underset{\sim}{k_p} = k_p \hat{\gamma} \qquad \underset{\sim}{k_s} = -k_s \hat{\beta} \tag{6}$$

The first four lines in Table 2 describe scattering in the $\gamma\beta$ plane. (The measured relative values in the last column are scaled so that the values for $\gamma(\alpha\alpha)\beta$ (row 1) both equal 80). Agreement between the spontaneous predicted and measured values in rows 2-4 is quite good in trend and reasonably good in magnitudes. The measured values in rows 2-4 are somewhat larger than predicted from the Z-cut crystal data and our model, but these numbers are small and less precisely measured with the exception of the 12.9 number in row 2. It is satisfying to see the measured value in row 4 is small, verifying that the (a-b) form of the scattering strength is valid. All in all, agreement is reasonable for scattering in the $\gamma\beta$ plane.

The situation is less simple for the $\gamma\alpha$ scattering plane, rows 5-8 in Table 2. For the polarized term, we measure a value half as large as predicted. In row 6, we again predict a very small strength, but measure 36.1. Similar behavior occurs in rows 7 and 8: one value is smaller than expected, the other larger. But note that the totals for fixed input polarization direction, indicated by brackets in Table 2, agree very well. One can say that the total scattering strength for input E-field polarized along β (that is, $\gamma(\beta\beta)\alpha$ plus $\gamma(\beta\gamma)\alpha$) agrees with prediction; likewise for incident E-field polarized along α. The results in rows 5-8 clearly indicate another angular variation of tensor elements (a and b, we think) that is not yet taken into account. The upshot of this for practical considerations for Nova is that, in the final considerations of measured stimulated gain (section II), we may expect to see similar "averaging" of the polarized and depolarized gain coefficients.

II. MEASUREMENTS OF ABSOLUTE SRS GAIN COEFFICIENTS

The absolute measurements of the stimulated gain coefficient g were made using two lasers - the Cyclops laser to provide the intense pump pulse, and a tunable cw dye laser to probe the gain at the Stokes frequency. The experimental layout is shown in Fig. 7. The 1053-nm Cyclops beam, of up to 5 J energy and at 1.1 ns duration, is frequency doubled in Type II KDP. The remanent infrared energy is absorbed in the dump D. Using mirrors M5 and M6, the pulsed beam is put on the axis defined by crosswires C3 and C5, with the sample out of the beam. Crosswire C4 is then put on this same axis at the location where the center of the sample will be placed. The cw dye laser is then skimmed past mirror M5 and, with mirrors M2 and M3, made to exactly intercept crosswire C4. The crossing angle of the two beams is 0.5°. When the KDP sample is put in place, the internal crossing angle is 1/3°.

Before we arrived at this angled-crossing arrangement, we tried to use an exactly collinear set-up. Prisms were used to refractively combine and later separate the pump and probe beams. This set-up had to be abandoned because of solarization of the prisms by the pump pulses. Prisms with dispersion strong enough to be useful showed solarization; fused silica, etc., prisms were too weakly dispersive.

The 526.5-nm pump beam is of $\sim$ 25 mm transverse diameter and is essentially flat over its central 10 mm. The dye-laser probe beam is less than 2 mm in diameter and, taking into account the small crossing angle, the cylinder of KDP that is probed by the sample beam is less than 3 mm in diameter. Over the central 3 mm, the pump beam is, to an

excellent approximation, flat. Hence, our fluence measurements could be made simply by using a 3-mm aperture (A1) in front of the absorbing-glass calorimeter (CAL), and dividing the indicated energy by the area of the aperture. The aperture was located at the distance optically equivalent to that of the sample center.

Because the cw probe was necessarily coincident with the pulsed beam at the calorimeter, it was necessary to reject that wavelength with an interference filter. We then calibrated the calorimeter shown if Fig. 7 with a second absorbing-glass calorimeter located in place of the sample. This calibration was performed at the beginning and at the end of a measurement run. We incurred no additional errors with this procedure.

Among the many laser lines of argon is 528 nm, and we were able to use this output of the laser (AL in Fig. 7) as a time-saving alignment substitute for the pulsed beam. Kinematically-mounted mirrors M1 and M4 were used to align the 528-nm beam onto crosswires C1 and C4, equivalent to C3 and C5.

The cw probe beam was generated by a Coherent Radiation CR-599 dye laser, pumped by a Spectra-Physics 171 cw argon laser. All the wavelengths needed for this work were obtained with a single dye, Rhodamine 110. The dye laser was equipped with frequency-stabilizing, single-mode electronics (FS in Fig. 7) giving a spectral width of less than 4×10^{-4} Angstroms. The probe wavelength was monitored with a wavemeter and, as backup, a scanned grating spectrograph. The precision of the wavemeter was better than 0.01 Angstroms, more than adequate for

this work. It was a time and frustration saver, because it gives a continual readout of wavelength without the need to incessantly scan, as with the grating instrument.

After passing through the sample, the probe beam was spatially separated from the pump and detected with a biplanar photodiode (D1). A major challenge in this measurement was the removal of the 526-nm pump light, eleven orders of magnitude more intense than the probe, from this 5531-nm detector channel. Filters F2, F3, F4, and apertures A2, A3, and A4, and numerous baffles were required. Aperture A2 (7 mm) was used to prevent as much pump light as possible from entering the KDP, because the KDP Tyndal-scattered a considerable amount of pump light from internal imperfections.

By the time the probe beam reached the detector D1, it was able to give a cw signal of about 10 mV on the scope S1. Considerable effort was spent maximizing this signal. We got the highest signal from the photodiode by removing the customary ground-glass scatterer and using a diverging lens to illuminate the full 2-inch diode surface. The diode signal was recorded on a Tektronix 7104 oscilloscope.

The other major experimental challenge in this work was to reduce all sources of spurious electrical noise on the scope traces to below 1 mV, so as not to cripple the signal/noise of the SRS gain measurement. It was necessary to put the diode detector, scope, and the trigger diode D2 in a copper-screen box, isolated from the metal optical table on which it sat, and that in turn isolated all other surrounding equipment. Furthermore, it was necessary to assemble a 1.5 kV supply for the diodes

from batteries, so as to eliminate additional connections to the outside world. All this done, we had a cw-diode signal that was acceptably quiet during the firing of the laser such that we could see with fidelity the Raman-gain-induced bump on the trace.

We choose to measure the absolute gain in liquid benzene, as a test of the operation of our apparatus. While the credibility of literature data on the absolute gain for benzene is far from adequate, it is as good as there is. Also, the 992 cm^{-1} mode in benzene can be conveniently reached with the same dye as for the 915 cm^{-1} mode of KDP. Fig. 8a is an example of the raw oscillogram data at 2 ns/div from our benzene (1-cm cell length) measurements. The lower trace shows the zero-line, and the upper trace shows a gain of 4.3. Fig. 8b is from a shot through the 15-cm KDP sample, and shows a 3.1 gain. The temporal waveform of the SRS signal follows that of the pump pulse.

At the beginning and end of each experimental run, "null" shots were taken with the dye probe beam blocked, and at pump intensities at least as high as the shots with the sample in place. This was for the purpose of proving that none of the observed gain signal was due to scattered pump light from imperfections inside a particular sample or from optical breakdown in any part of the apparatus or sample.

For both benzene and KDP, the frequency of the dye probe beam was scanned and shots were taken to plot out SRS gain versus frequency. The experimental data for these spectral runs are displayed in Fig. 9 for benzene and KDP. This made sure we covered the exact probe wavelength for which the SRS gain was maximum. This procedure was more important

for benzene than for KDP, due to the 8.7x narrower benzene line. It is satisfying to see that the width of the benzene line from our direct stimulated gain measurements, 2.3 cm^{-1}, is the same as that published in Skinner and Nilson's[12] careful spontaneous work. The width of the KDP stimulated gain line, 20 cm^{-1}, is also in reasonable agreement with our earlier spontaneous measurements.

Our results, first for the absolute gain in benzene, are listed in Table. 3. The gain available from the 1-cm path length is entirely sufficient for quality measurements (see Fig. 8). For substantiation that the gain coefficient from this data was not compromised by self-focusing, we measured the gain for two longer cell lengths of benzene also. From Table 3, we see that the 1- and 2-cm cell lengths gave essentially the same result, but the 5-cm cell did not. From the literature, the B-integral for benzene is $\sim$ 1 rad per centimeter of path length, for 0.4 GW/cm^2 input intensity. So the 1-cm number for g in Table 3 is not appreciably affecte by self-focusing of the flat-profile pump beam. It is difficult to guess which of the other available nonlinearities caused the gain coefficient for 5 cm to deviate, and that is of no consequence. The value 4.3 cm/GW for 526.5-nm pump is our result. The absolute uncertainty in this number is ± 20%. This measurement is the most credible absolute SRS gain coefficient in existence, in our opinion. Referring to Table 4, we see that it is, incidentally, in excellent agreement with the previous two estimates from stimulated work, and with the several computations from spontaneous parameters.

This situation leads us to say that, for future surveys of SRS strength in materials such as advanced harmonic generation materials, it is valid - at least for a first cut - to run the spontaneous spectrum and scale the gain with the above absolute number. If particular modes of interest are nonsimple - eg., overlapping modes, polariton character, or anomalous dependence on scattering k vectors - additional work will be required.

The results for the measured absolute gain in KDP are listed in Table 5. Two different lengths of KDP were tested - 5 and 15 cm. Both crystals were spare KDP array segments. We propagated our test beams through the edge faces of these crystals. Hence the Raman probe beam in these tests propagates just as would the Raman wave in the actual array. The pump beam also travels in this direction, near-collinear with the probe beam as previously described. This is transverse to the pump direction encountered in the array geometry.

The first column in Table 5 indicates the scattering geometry referenced to Fig. 5. The third column shows the particular combination of scattering tensor elements involved for the stimulated gain measurement. Our approach to predicting the Raman gain coefficients was to arrive at "best" values of the diagonal Raman tensor elements, a^2 and b^2, from direct stimulated gain measurements, and then to compute the coefficients from tensor couplings listed in Table 2, appropriate for the transverse pump geometry. For a^2 a "best" value of 0.21 cm/GW was determined as an average of results for the 5 and 15 cm crystals from configuration $\bar{\beta}(\alpha\alpha)\bar{\beta}$. Configuration $\alpha(zz)\alpha$ used with the 5 cm

crystal directly gave a value of 0.13 cm/GW for b^2. The predicted SRS gain coefficients in Table 5 were calculated with the "best" a^2 and b^2 as above and are in good agreement with experiment. In particular, the gain coefficient 0.076 cm/GW for the depolarized scattering $\bar{\beta}(\alpha\gamma)\bar{\beta}$ is in excellent agreement with the experimental value of 0.065 cm/GW and substantiates our model for the $\epsilon(\psi)$ tensor element, Eq. 4. In the array geometry, an extraordinary wave polarized along $\hat{\beta}$ will principally scatter into direction $\hat{\alpha}$ (or $-\hat{\alpha}$). From Table 2 the appropriate tensor coupling for configuration "e" = $\gamma(\beta\beta)\alpha$ is $[a\cos^2\theta+b\sin^2\theta]^2$. With "best" values for a^2 and b^2 this gives a gain coefficient of 0.15 cm/GW. Thus, the major results are that the KDP SRS gain coefficient for 526.5-nm pump is 0.21 cm/GW when the scattered wave is an "o" wave in the crystal, and is 0.15 when it is an "e" wave. These results are expanded in Table 6 with error bars for ω, 2ω, 3ω, and 4ω wavelengths relevant for Nova/Novette.

III. SRS LOSS IN NOVA/NOVETTE ARRAYS

We now use the gain coefficients from the previous section to re-examine the risk to the Nova/Novette arrays that is posed by SRS in KDP. Using the gain coefficients from Table 6 and the current Nova maximum intensity data (Table 7), we arrive at the single pass gain for the various waves involved in doubling and tripling. These values are collected in Table. 8 for ω through 4ω, and they are all too low to cause problems on a single pass.

It remains to compute the loss for long pulses, which allow multiple traversals of the KDP segments. Using the same code as in our previous

analysis, we considered the SRS loss for metal-eggcrate arrays, arrays with no eggcrate, and arrays with absorbing glass partitions, for both 15- and 27-cm crystal segments. The criterion for unacceptable loss in all cases was the side-scatter of 1 % of the incident intensity. These results are listed in Table 9. The left blocks in this Table are calculated using gain factors from Table 6. The center and right blocks indicate the effect of the ± 20% error bar on the gain coefficient. In this Table, "safe" and "unsafe" are abbreviated S and U. U^* means unsafe, but only over a small subset of the parameter space involving pulse duration, edge reflectivity, and spontaneous noise source intensity.

In our computations, the only differences between metal eggcrate, no eggcrate, absorbing glass partitions are the numbers used for the edge reflectivity and the crystal transverse size. For the metal case, reflectivities of 90, 50, and 10 percent were used; for no eggcrate, 100% was used; for the glass partitioned array, 1, 0.5, and 0.1 percent were used. For transverse size in the no-eggcrate case, 70 cm clear aperture was used.

Let us first discuss the results at the second-harmonic frequency. USING THE DIRECTLY MEASURED GAIN COEFFICIENT, THE GENERATION OF THE SECOND-HARMONIC IS SAFE FOR ALL THREE CONSIDERED TYPES OF ARRAY STRUCTURE. This is Part A of the BOTTOM LINE of this memorandum. Considering the upper end of the error bar (1.2 x G) for the second harmonic, we see that the no-eggcrate array is unsafe. The absorbing glass partitioned array is safe. The metal eggcrate array is "almost" safe: that is, for a limited range of pulse duration and for pessimistic

assumptions of edge reflectivity and noise intensity source, SRS side-scatters more than 1% of the incident intensity. Since we have no actual stimulated Raman measurements on an array yet, we do not know what value of noise intensity, etc., is accurate.

Next, we look at the results for the third harmonic. USING THE MEASURED GAIN COEFFICIENT, WE INDICATE THAT THE ARRAY CAN PROPERLY TRANSMIT THE DESIRED 3ω INTENSITY ONLY IF ABSORBING GLASS PARTITIONS ARE EMPLOYED. This is Part B of the BOTTOM LINE of this memo. Even with the lower edge of the uncertainty bar on the gain coefficient, the no-eggcrate design has a problem, and the metal eggcrate design a restricted problem at 3ω. For the upper end of the error bar, even the absorbing-glass-partitioned array may have a restricted problem with the 27-cm crystals.

We included in Table 8 the numbers relevant for Type-I fourth-harmonic generation in KDP. The gain coefficient at 4ω was scaled by ω_s from the 2ω measured values, as usual. The pump intensity was put at 2 GW/cm^2 maximum, and 1 GW/cm^2 maximum output at 4ω was assumed, for a starting point. With these low intensity values, SRS at 4ω, or by the 2ω pump, appears to not be a problem. It should be mentioned here that we have no way to estimate pre-resonant effects which could make the 4ω gain coefficients considerably larger.

The problems indicated above occur only for long pulse durations. For the second-harmonic, we indicate problems only for pulse durations longer than 3 ns, and for the third-harmonic, only beyond 2 ns. It is interesting to note that, for pulse durations longer than about 2 ns, the

current, redesigned Nova output intensities listed in Table 7 are higher than the original Nova baseline numbers . We see that this increased performance can be had at the third-harmonic only if absorbing glass partitions (or some other effective SRS suppressor) are incorporated in the tripling arrays.

ADDITIONAL WORK

It is now necessary that we examine the SRS in an actual Novette array, for confirmation in situ of the results presented here and to see the effects of other remaining uncertainties, which are the effective noise source intensity and the effect of the particular optical geometry of the array (total internal reflection, etc.) on the growth of SRS. We will work with Nova staff to draw up a proper plan and schedule for the work. The array diagnostics should be placed in working order such that the first Novette 2ω pulses at 1 ns or longer can be monitored.

SUMMARY

- SRS should not hamper Novette array performance at 2ω.

- If third-harmonic generation were attempted on Novette with metal-eggcrate arrays, it would probably fail for pulses longer than $\sim$ 2 ns. Failure here means exponentially-growing loss of energy and probable damage, possibly catastrophic, to the tripler arrays.

- Absorbing glass partitions (or some other effective SRS suppressant) appear to be required for the tripler arrays on Nova. They may be needed as insurance for the doubler arrays.

- No-eggcrate designs, such as the corner-glass-cross concept, will be safe at 2ω and fail at 3ω.

- Examination of SRS in the Novette arrays will be required to tie down the remaining uncertainties.

- We have described a distinct limitation to the maximum useful size of a crystal segment in a crystal array. Plans for growing still larger crystals should be altered to concentrate on better volume or yield rather than additional cross-sectional area.

February 25, 1983

References

1. W. L. Smith and F. P. Milanovich, "Stimulated Raman Scattering Inside KDP Segments", Memo UVM 82-19, August 25, 1982.
2. D. K. Agrawal and C. M. Perry, in Proceedings of the Second International Conference on Light Scattering in Solids, (Flammarion Sciences, Paris, 1971), p. 429.
3. N. Toupry-Zrauzman, H. Poulet, and M. LePostollec, J. Raman Spectr. 8, 115 (1979).
4. J. West, Z. Krist. 74, 306 (1930).
5. G. Herzberg, Molecular Spectra and Molecular Structure (van Nostrand Reinhold, New York, 1945) p. 100.
6. B. C. Fraser and R. Pepinsky, Acta. Cryst. 6, 273 (1953).
7. M. K. Srivastava and R. W. Grow, Optics Comm. 8, 82 (1973); note that the gain coefficients in Table 1 of this paper are misprinted 10x too large. (See "Studies on the Tunability of the Stimulated Raman Effect due to Polaritons in GaP and KH_2PO_4 Crystal", by M. K. Srivastava and G. W. Grow, Report UTEC MD 73-057, Microwave Device and Physical Electronics Laboratory, Univ. of Utah, March, 1973).
8. M. K. Srivastava and R. W. Grow, and C. H. Wang, Chem. Phys. Lett 26, 157 (1974).
9. M. K. Srivastava and C. H. Wang, J. Chem. Phys. 62, 3439 (1975).
10. M. K. Srivastava, C. H. Wang, and R. W. Grow, Chem. Phys. Lett. 35, 264 (1975).

11. E. A. Popova and A. I. Stekhanov, Soviet Physics-Solid State 12, 40 (1970).

12. J. G. Skinner and W. G. Nilson, J.O.S.A. 58, 113 (1968).

13. F. Aussenegg and U. Deserno, Opt. Commun. 2, 295 (1970).

14. M. J. Colles, Opt. Commun. 1, 169 (1969).

15. G. G. Bret and H. P. Weber, IEEE J. Quant. Electr. 4, 807 (1968).

16. J. B. Grun, A. K. McQuillan, and B. P. Stoicheff, Phys. Rev. 180, 61 (1969).

17. F. J. McClung, W. G. Wagner, and D. Weiner, Phys. Rev. Lett. 15, 96 (1965).

18. W. D. Johnston, Jr., I. P. Kaminow, and J. G. Bergman, Appl. Phys. Lett. 13, 190 (1968).

Table 1. Measured Spontaneous Raman Scattering Strengths for Z-cut KDP Crystal

Scattering Configuration	Tensor Coupling	Ψ (deg)	Scattering Strength†	Scattering Configuration	Tensor Coupling	Ψ (deg)	Scattering Strength†
			scattering in xy plane				
x(zz)y	b^2	90	82.0	$\bar{y}(zz)x$	b^2	90	80.5
x(yx)y	$c(\Psi)^2$	90	2.5	$\bar{y}(xy)x$	$c(\Psi)^2$	90	2.7
x(zx)y	d^2	90	5.0	$\bar{y}(xz)x$	d^2	90	1.6
x(yz)y	e^2	90	2.0	$\bar{y}(zy)x$	e^2	90	5.0
			scattering in xz plane				
$x(yy)\bar{z}$	a^2	46.4	72.5	z(yy)x	a^2	43.6	79.0
$x(yx)\bar{z}$	$c(\Psi)^2$	46.4	24.0	z(xy)x	$c(\Psi)^2$	43.6	25.0
$x(zx)\bar{z}$	d^2	46.4	3.5	z(xz)x	d^2	43.6	4.1
$x(zy)\bar{z}$	e^2	46.4	2.7	z(yz)x	e^2	43.6	5.5
			scattering in yz plane				
$\bar{y}(xx)\bar{z}$	a^2	46.4	95.0	$z(xx)\bar{y}$	a^2	43.6	79.5
$\bar{y}(xy)\bar{z}$	$c(\Psi)^2$	46.4	34.5	$z(yx)\bar{y}$	$c(\Psi)^2$	43.6	25.0
$\bar{y}(zx)\bar{z}$	d^2	46.4	3.1	$z(xz)\bar{y}$	d^2	43.6	6.0
$\bar{y}(zy)\bar{z}$	e^2	46.4	3.9	$z(yz)\bar{y}$	e^2	43.6	4.2

† arbitrary units; measurement precision ± 5%.

Table 2. Predicted and Measured Spontaneous Raman Scattering Strengths for Type II ($\Theta = 59°$) KDP Crystal (90°-scattering)

Scattering Configuration	Tensor coupling	Approximate Tensor Coupling	Ψ (deg)	Spontaneous Scattering Strength† predicted		Spontaneous Scattering Strength† †† measured	
1. $\gamma(\alpha\alpha)\bar{\beta}$	a^2	a^2	102.6	80.0		80.0	
2. $\gamma(\alpha\gamma)\bar{\beta}$	$[c(\Psi)\sin\Theta+d\cos\Theta]^2$	$[c(\Psi)\sin\Theta]^2$	102.6	1.9		12.9	
3. $\gamma(\beta\alpha)\bar{\beta}$	$[c(\Psi)\cos\Theta-d\sin\Theta]^2$	$[c(\Psi)\cos\Theta]^2$	102.6	0.7		2.6*	
4. $\gamma(\beta\gamma)\bar{\beta}$	$[1/2(a-b)\sin2\Theta+e\cos2\Theta]^2$	0**	102.6	0**		3.4*	
5. $\gamma(\beta\beta)\alpha$	$[a\cos^2\Theta+b\sin^2\Theta-e\sin2\Theta]^2$	a^2	68.1	80.0	80.0	36.6	72.7
6. $\gamma(\beta\gamma)\alpha$	$[1/2(a-b)\sin2\Theta+e\cos2\Theta]^2$	0**	68.1	0**		36.1	
7. $\gamma(\alpha\beta)\alpha$	$[c(\Psi)\cos\Theta-d\sin\Theta]^2$	$[c(\Psi)\cos\Theta]^2$	68.1	2.0	7.5	4.4*	9.0
8. $\gamma(\alpha\gamma)\alpha$	$[c(\Psi)\sin\Theta+d\cos\Theta]^2$	$[c(\Psi)\sin\Theta]^2$	68.1	5.5		4.6*	

† arbitrary units

†† precision, ± 5%

* precision, ± 30%

** this value is proportional to the difference a-b, which we have approximated to be zero.

Table 3. Measured SRS gain for 992 cm^{-1} mode of benzene.
Pump wavelength = 526.5 nm

Cell Length (cm)	Pump Intensity Range (GW/cm^2)	Benzene SRS Gain Coefficient g (cm/GW)
1	0.31 - 0.39	4.3
2	0.12 - 0.23	4.5
5	0.04 - 0.07	3.8

Best g value for benzene with 526.5-nm pump:

4.3 ± 0.9 cm/GW

Table 4. Literature values of stimulated Raman gain coefficient g for benzene 992 cm^{-1} vibrational mode.

Authors	pump λ (nm)	SRS g at pump λ (cm/GW)	SRS g at 488-nm pump (cm/GW)	Comments
Aussenegg et al.[13]	532.	5	5.5	estimate from measurement of stimulated Raman threshold
Colles[14]	532.	∿ 5	∿ 5.5	estimate from stimulated conversion of power to the Stokes frequency
Colles[14]	532.	5.2	5.7	computation from spontaneous data
Bret & Weber[15]	532.	4.5	4.9	" "
Grun et al.[16]	694.3	2.8	4.1	" "
McClung et al.[17]	694.3	3.8	5.5	" "
Johnston et al.[18]	1064.	2.7	6.3	" "
Skinner & Nilson[12]	694.3	3	4.4	" "
This work	526.5	4.3±0.9	4.7±0.9	direct measurement in small gain regime with single-frequency lasers.

Table 5. Measured absolute SRS gai.. coefficients for 915 cm^{-1} mode of KDP, with predictions using our theoretical model.

Scattering Configuration	Length (cm)	Tensor Coupling	Approximate Tensor Coupling	Ψ (deg)	Predicted SRS Gain Coefficient†	Measured SRS Gain Coefficient (cm/GW)
1. $\beta(\alpha\alpha)\beta$	5	a^2	a^2	31	0.21	0.23
2. $\beta(\gamma\gamma)\beta$	5	$[a\sin^2\theta+b\cos^2\theta+e\sin 2\theta]^2$	$[a\sin^2\theta+b\cos^2\theta]^2$	31	0.19	0.19
3. $\alpha(\gamma\gamma)\alpha$	5	$[a\sin^2\theta+b\cos^2\theta+e\sin 2\theta]^2$	$[a\sin^2\theta+b\cos^2\theta]^2$	90	0.19	0.23
4. $\beta(\alpha\alpha)\beta$	15	a^2	a^2	31	0.21	0.19
5. $\beta(\alpha\gamma)\beta$	15	$[c(\Psi)\sin\theta+d\cos\theta]^2$	$[c(\Psi)\sin\theta]^2$	31	0.076	0.065
6. $\alpha(yy)\alpha$	15	a^2	a^2	90	0.21	0.19
7. $\alpha(zz)\alpha$	15	b^2	b^2	90	0.13	0.13
8. $\alpha(zy)\alpha$	15	e^2	0	90	0.0	0.065

† Normalized to 0.21 cm/GW for a^2 tensor coupling.

Table 6. Stimulated Raman Gain Coefficient in KDP at Nova/Novette Wavelengths

Pump λ (nm)	Direction of Pump Polarization in KDP "e"≡γ(ββ)α "o"≡γ(αα)β	Pump ω (cm^{-1})	ω_s (cm^{-1})	λ_s (nm)	Initial Prediction (UVM 82-19)	Direct Measurement;* This Work
1053	"e"	9,497	8,582	1165	0.10±0.05	0.071±0.027
1053	"o"	9,497	8,582	1165	0.20±0.10	0.10 ±0.02
526.5	"e"	18,993	18,078	553	0.21±0.10	0.15 ±0.03
526.5	"o"	18,993	18,078	553	0.43±0.22	0.21 ±0.04
351	"e"	28,490	27,575	363	0.33±0.17	0.23 ±0.05
351	"o"	28,490	27,575	363	0.65±0.33	0.32 ±0.06
263.3	"e"	37,987	37,072	270	-	0.31 ±0.06
263.3	"o"	37,987	37,072	270	-	0.43 ±0.09

* values scaled for frequency according to g proportional to ω_s

Table 7. Nova Maximum Output Intensity (GW/cm^2) with Redesigned Output Stage, as of 1/28/83†

Pulse Duration (ns)	ω	2ω	3ω
0.5	3.72	3.25	2.95
1.0	3.17	2.74	2.56
1.5	2.80	2.36	2.26
2.0	2.52	2.08	2.02
2.5	2.28	1.86	1.80
3.0	2.16	1.67	1.67
3.5	1.91	1.52	1.48
4.0	1.77	1.38	1.36
4.5	1.65	1.27	1.26
5.0	1.57	1.19	1.15

† W. W. Simmons, M. A. Summers

Table 8. Revised (1/31/83) Short-Pulse Parameters for Stimulated Raman Scattering in 27-cm and 15-cm KDP Segments at Nova Intensity Levels. In this pulse-duration range, SRS is limited to $\leq$ 1 traversal of the KDP segment.

lumn	1	2	3	4	5	6	7	8	9
	PUMP WAVE	PUMP WAVE ORIENTATION†	NOVA MAX INTENSITY I_m inside KDP (GW/cm^2)			SRS g (cm/GW)	$G = gI_m L_{eff}$		
			1.0 ns	1.35 ns	0.75 ns		1.0 ns L_{eff}=20 cm	1.35 ns L_{eff}=27 cm	0.75 ns L_{eff}= 15 cm
	ω in Type I SHG	"o"	3.18	2.91	3.43	0.10	6.4	7.9	5.1
	2ω in Type I SHG	"e"	2.74	2.46	2.98	0.15	8.2	10.0	6.7
	Half the ω in Type II SHG	"e"	1.59	1.45	1.71	0.071	2.3	2.8	1.8
	Half the ω in Type II SHG	"o"	1.59	1.45	1.71	0.10	3.2	3.9	2.6
	2ω in Type II SHG	"e"	2.74	2.46	2.98	0.15	8.2	10.0	6.7
	ω in Type II THG	"e"	1.06	0.97	1.14	0.071	1.5	1.9	1.2
	2ω in Type II THG	"o"	2.12	1.94	2.29	0.21	8.9	11.0	7.2
	3ω in Type II THG	"e"	2.56	2.35	2.73	0.23	11.8	14.6	9.4
	2ω in Type I 4HG	"o"	2.0	2.0	2.0	0.21	8.4	11.3	6.3
	4ω in Type I 4HG††	"e"	1.0	1.0	1.0	0.31	6.2	8.4	4.7

"e" $\equiv \gamma(\beta\beta)\alpha$; "o" $\equiv \gamma(\alpha\alpha)\beta$

this extrapolation of gain coefficients to 4ω ignores all possible pre-resonant enhancement.

Table 9. RISK TO HARMONIC ARRAYS FROM SRS IN KDP.

crystal size (cm)	G			Gx1.2			Gx0.8		
	SECOND HARMONIC								
	ME	N	AGP	ME	N	AGP	ME	N	AGP
15	S	S	S	U*	U	S	S	S	S
27	S	S	S	U*	U	S	S	S	S
	THIRD HARMONIC								
	ME	N	AGP	ME	N	AGP	ME	N	AGP
15	U	U	S	U	U	S	U*	U	S
27	U	U	S	U	U	U*	U*	U	S

ME=metal eggcrate N=no eggcrate AGP=absorbing glass partitions

S=safe U=unsafe U*=unsafe for limited subset; see text

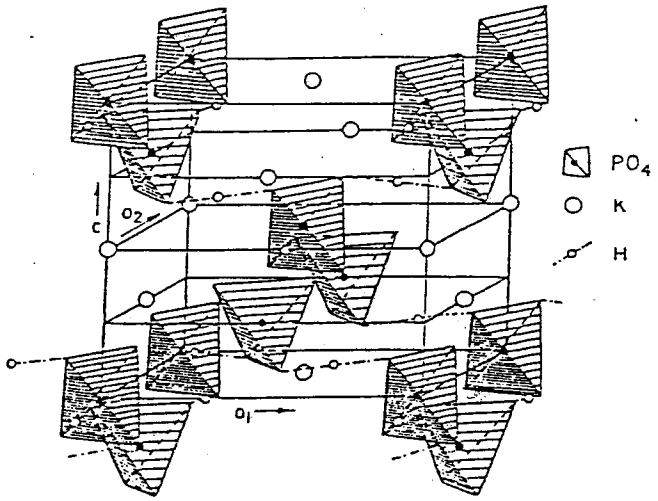

Figure 1: Unit cell of KH_2PO_4 (Ref. 4).

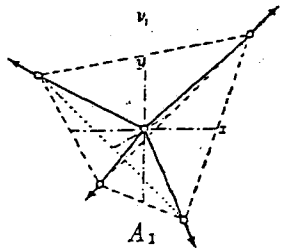

Figure 2: Motion of the oxygen atoms relative to the phosphorous atom in the ν_1-mode of the free PO_4 tetrahedron (Ref. 5).

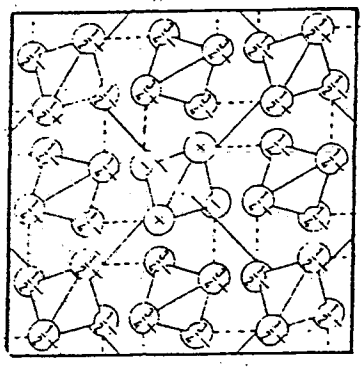

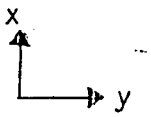

Figure 3: Illustration of the locations of the H_2PO_4 sub-systems in the KH_2PO_4 unit cell. View is looking down the c axis. The dashed lines represent OHO bonds which interconnect the PO_4 tetrahedra. For clarity the potassium atoms are not shown. The numbers inside the oxygen symbols (circles) indicate the fractional depth of the location along the z-axis in the unit cell. (Taken from x-ray work of B. C. Frazer, Ref. 6).

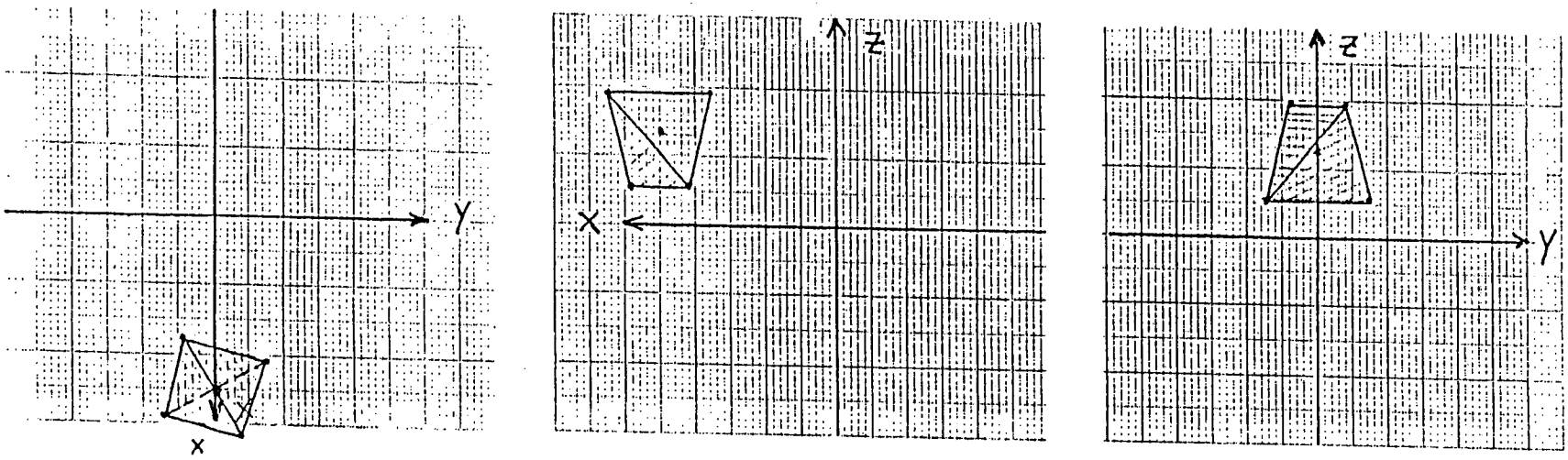

(a) (b) (c)

Figure 4: Views of a PO_4 tetrahedron in the xy, xz, and yz planes, illustrating that the steric rotation, due to OH bonding, is about the z-axis only (atomic coordinates from Ref. 6).

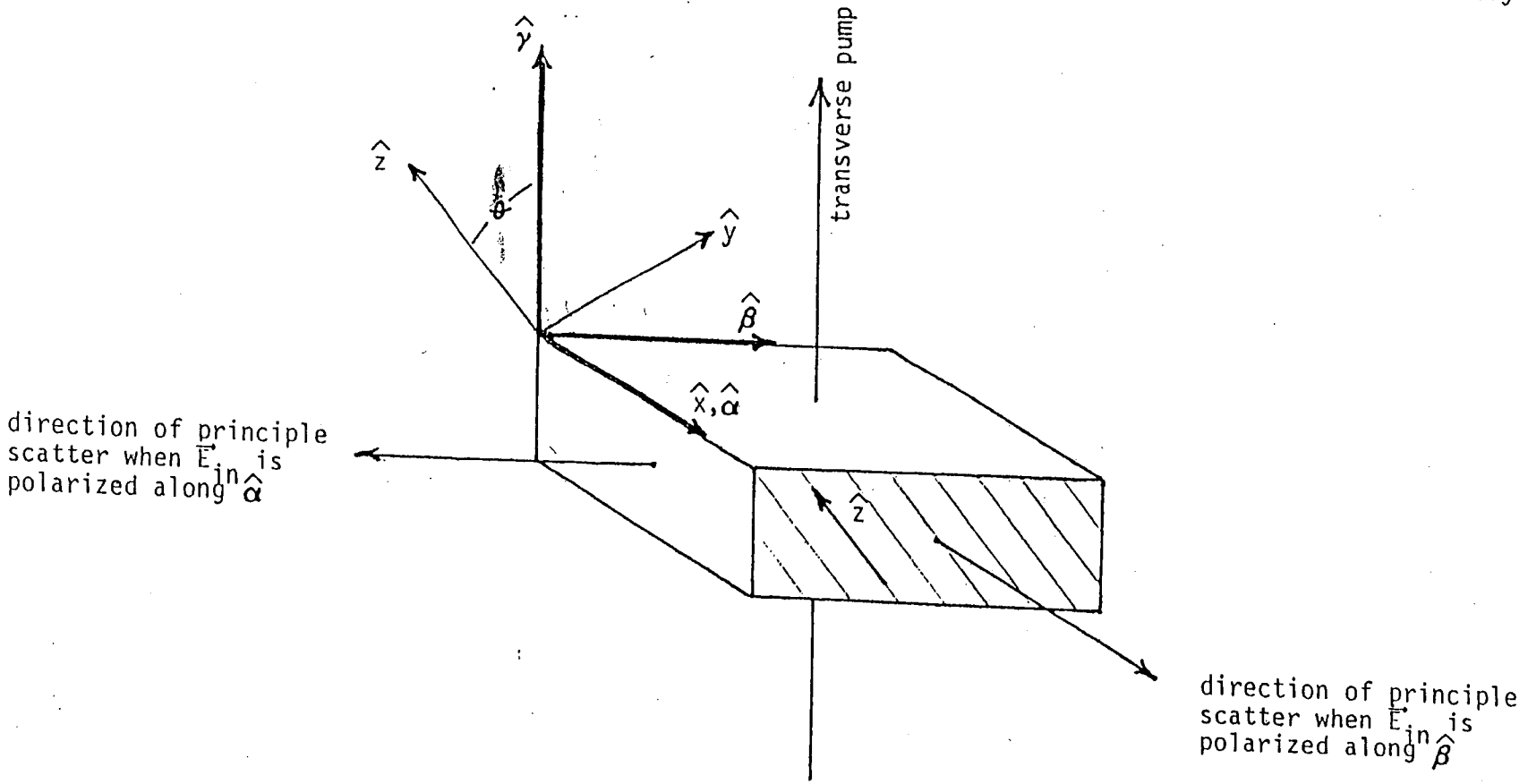

Figure 5: Labels for axes of KDP: x, y, z are crystal axes, α, β, γ are laboratory axes.

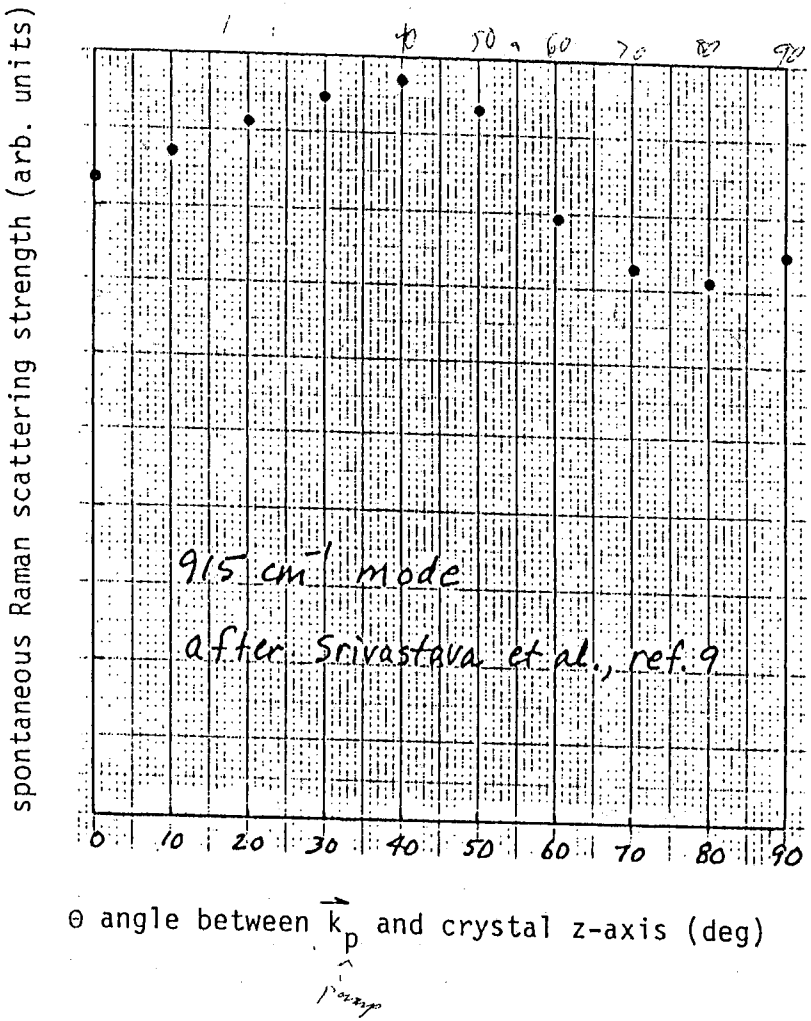

Figure 6: Angular variation of polarized Raman scattering strength in KDP.

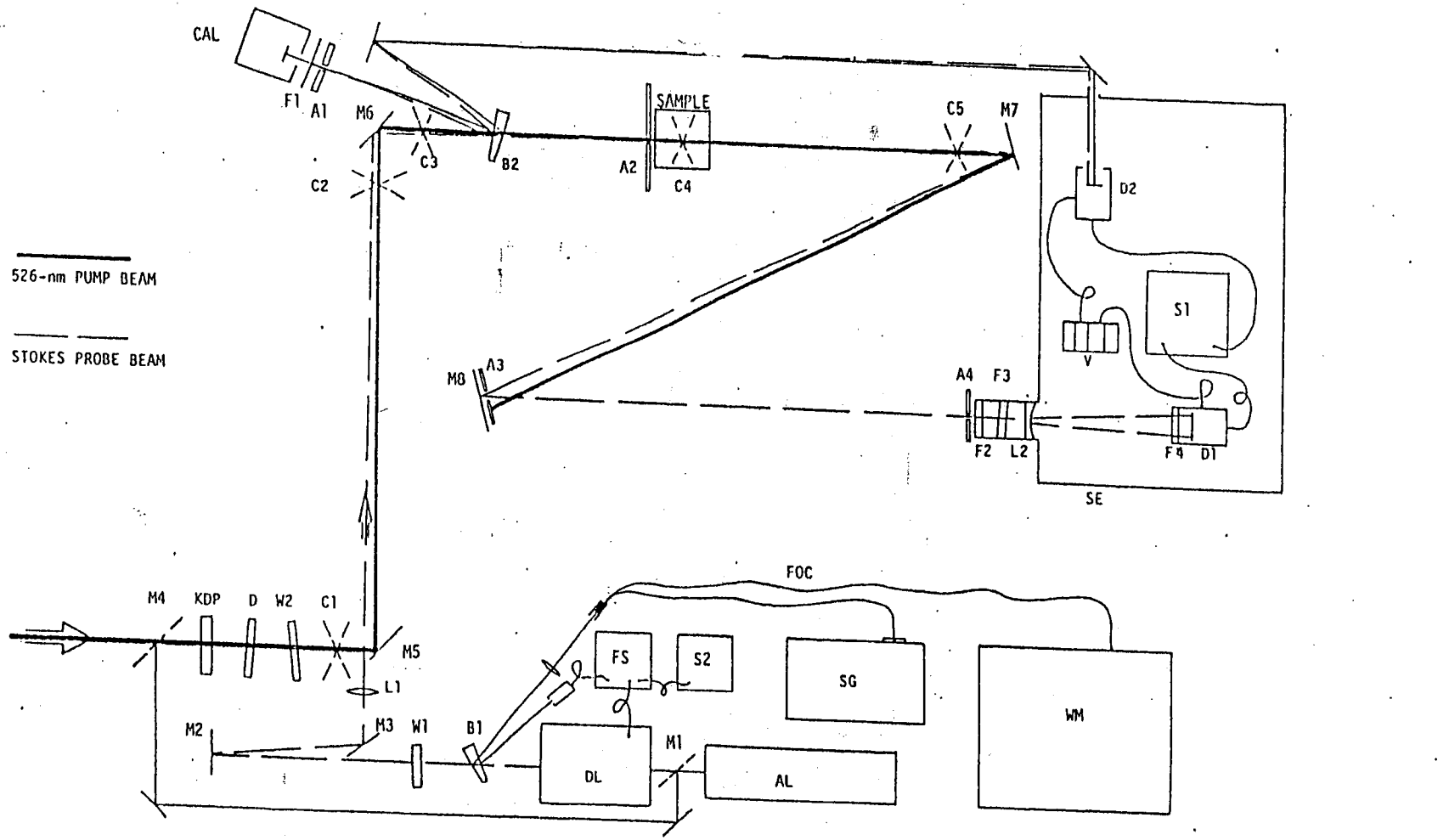

LEGEND: A1-A4, apertures; AL, argon laser; B1-B2, wedged beamsplitters; C1-C5, removable alignment cross-wires; CAL, absorbing-glass calorimeter; D1-D2, S-20 biplanar photodiodes; D, absorbing-glass dump for 1053-nm laser; DL, single-mode dye laser; F1, band-pass filter for 526 nm; F2-F4, filters to pass only the Stokes beam; FOC, fiber-optic light leads; FS, frequency scanning and stabilization electronics; KDP, doubling crystal; L1, imaging lens; L2, diverging lens; M1-M8, reflecting mirrors (M1 and M4 are removable); S1, Tektronix 7104 oscilloscope; S2, oscilloscope for frequency monitoring; SE, copper-shielded enclosure for detector; SG, 1-m scanning spectrograph; V, voltage supply (1.5 kV battery); W1-W2, half-wave plates; WM, optical wavemeter.

Fig. 7: EXPERIMENTAL APPARATUS FOR STIMULATED GAIN MEASUREMENT.

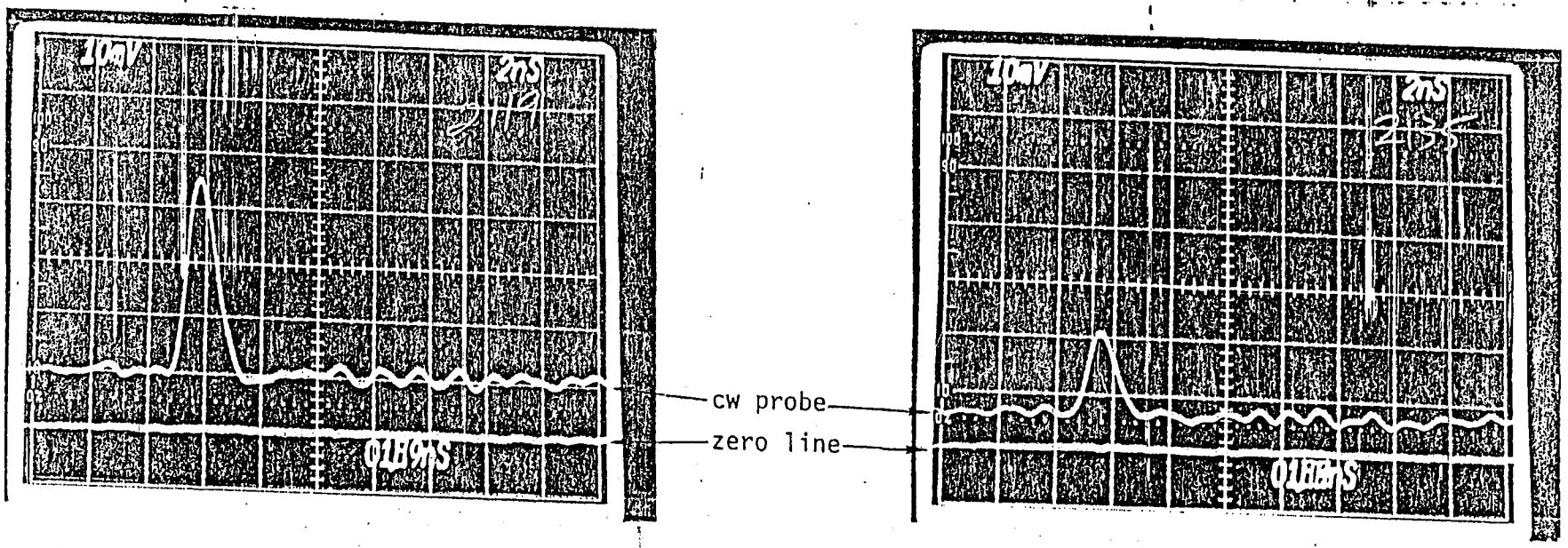

a. Benzene, 1-cm path length;
gain = 4.3 ± 0.3

b. KDP, 15 cm path length;
gain = 3.2 ± 0.3

Figure 8: Oscillograms showing stimulated Raman gain on a cw probe beam. The lower trace on each photograph is the zero-line.

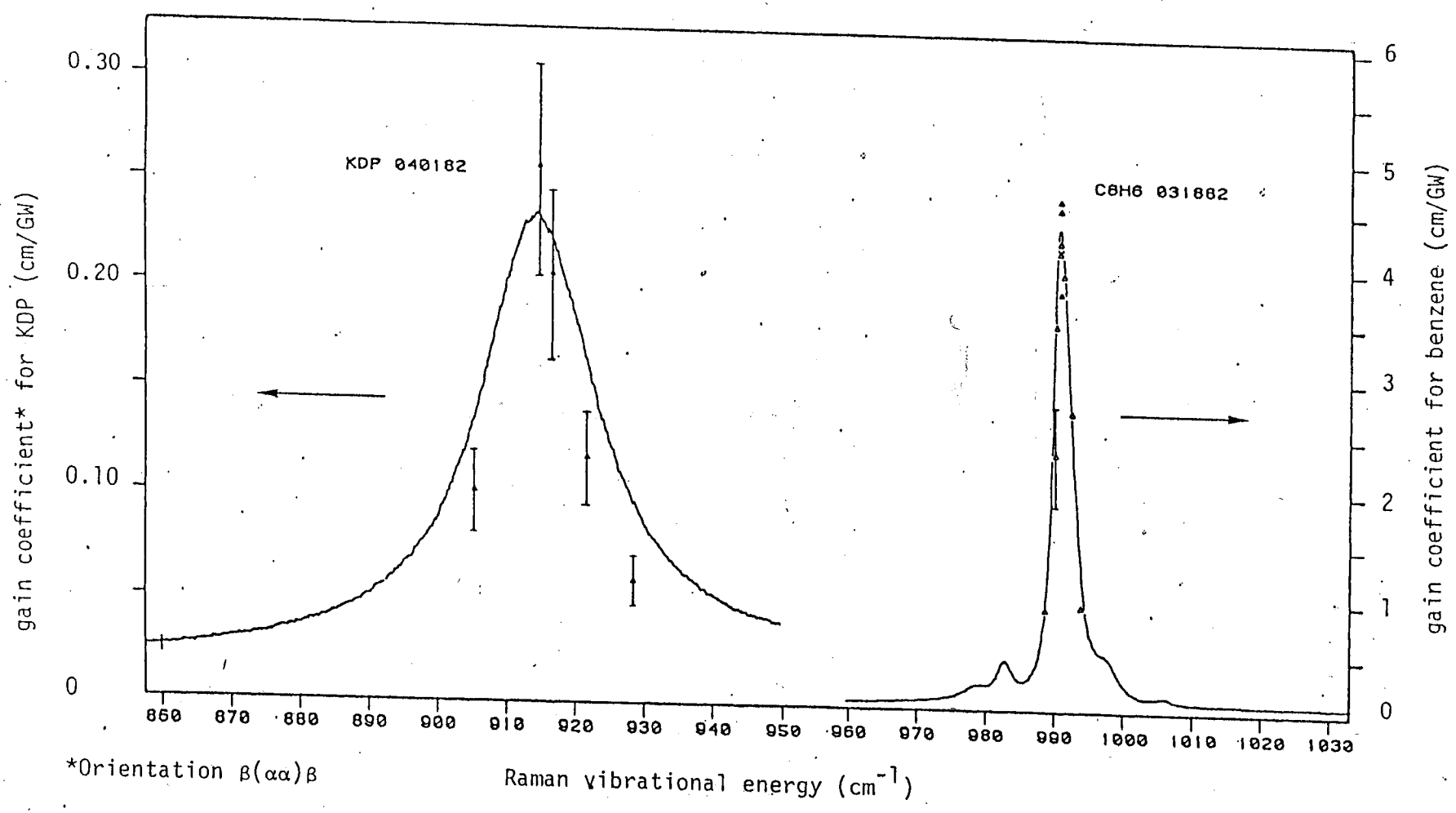

Figure 9: SRS gain coefficient versus wavelength. The data points are from absolute measurements and they are overlaid on the spontaneous Raman spectra. The vertical scales are different for the two materials.

Distribution

Ahlstrom, H. G.	L-481
Attwood, D. T.	L-473
Bender, C. F.	L-326
Bliss, E. S.	L-492
Campbell, E. M.	L-473
Coleman, L. W.	L-473
Eimerl, D.	L-487
Emmett, J. L.	L-488
Godwin, R. G.	L-493
Goldhar, J.	L-490
Haas, R. A.	L-487
Hagen, W. F.	L-490
Hopper, R.	L-490
Holzrichter, J. F.	L-481
Hunt, J. T.	L-487
Kan, T.	L-467
Krupke, W. F.	L-488
Kushner, M.	L-490
Lindl, J.	L-477
Lowdermilk, H.	L-490
Manes, K.	L-493
Milam, D.	L-490
Murray, J. E.	L-490
Murray, J. R.	L-490
Nuckolls, J.	L-477
Pleasance, L. D.	L-487
Powell, H. T.	L-490
Simmons, W. W.	L-493
Sooy, W.	L-488
Speck, D. R.	L-493
Stokowski, S. E.	L-491
Summers, M. A.	L-493
Suski, G.	L-493
Trenholme, J. B.	L-487
Vercimak, C.	L-272
Wallerstein, E. P.	L-491
Warren, W. E.	L-490
Warshaw, S.	L-492
Weber, M. J.	L-490